Direct numerical simulation of turbulent heat transfer in a square duct

M. Piller and E. Nobile

Dipartimento di Ingegneria Navale, del Mare e per l'Ambiente Sezione di Fisica Tecnica, Università di Trieste, Trieste, Italy

Keywords *Numerical simulation, Turbulence, Heat transfer, Square cavity, Finite volume*

Abstract *The results from a direct numerical simulation (DNS) of turbulent, incompressible flow through a square duct, with an imposed temperature difference between the horizontal walls, are presented. The vertical walls are assumed perfectly insulated, and the Reynolds number, based on the bulk velocity and the hydraulic diameter, is about 4400. Our results indicate that secondary motions do not affect dramatically global parameters, like the friction factor and the Nusselt number, with respect to the plane-channel flow, but the distributions of the local shear stress and heat flux at the walls are highly non-uniform, due to the presence of these secondary motions. It is also shown that an eddy-diffusivity approach is capable to reproduce well the turbulent heat flux. All simulations were performed by an efficient finite volume algorithm. A description of the numerical algorithm, together with an analysis of time-accuracy, is included. The OpenMP parallel programming language was exploited to obtain a moderately-scalable application.*

Nomenclature

D_h = hydraulic diameter, $2h$
C_f = friction factor
h = half-height of the channel
H = height of the lid-driven cavity
$\boldsymbol{i}$ = unit vector for the streamwise coordinate
$\boldsymbol{j}$, $\boldsymbol{k}$ = unit vectors for the cross-flow coordinates
k = thermal conductivity
k_x = streamwise wave-number, $k_x = 2\pi k/l_x$
l_x = streamwise domain length
n = outer-directed wall-normal unit vector
N_x = number of cells in the streamwise coordinate
N_y, N_z = number of cells in the cross-flow coordinates
Nu = average Nusselt number
p = kinematic pressure
p^* = tentative kinematic pressure for Projection methods
Pr = Prandtl number, ν/α
q_y, q_z = modelled components of turbulent heat flux in the cross-flow plane
Re_b = bulk Reynolds number
Re_τ = Reynolds number, $u_\tau D_h/\nu$
t = time
t_f = time-interval for Projection schemes
t_K = Kolmogoroff's time-scale
T = temperature
T_w = wall-temperature
$\boldsymbol{u}$ = velocity vector
u, v = velocity components in the x and y directions, respectively
u_τ = friction-velocity, $u_\tau = \sqrt{\tau_w/\rho}$

Financial support for this research was provided by ENEA – Contract *Settore Calcolo* L. 95/95 – and by MURST – Progetto di Ricerca di Interesse Nazionale 1999, "Enhancement techniques in thermofluids", and is gratefully acknowledged. The calculations for case A have been performed on the IBM SP3 at the Centro di Calcolo dell'Università di Trieste.

International Journal of Numerical Methods for Heat & Fluid Flow, Vol. 12 No. 6, 2002, pp. 658-686.

DOI 10.1108/09615530210438346

u^* = intermediate velocity field
v = *projected* divergence-free velocity field
x = streamwise coordinate
x_i = generic coordinate
x_i^+ = wall units, $x_i\, u_\tau/\nu$
w = velocity imposed at the boundary
y, z = cross-flow coordinates

Greek

α = thermal diffusivity
α_t = turbulent thermal diffusivity
ΔS = surface of control volume
Δt = computational time-step
ΔT_w = wall-temperature difference
Δx = dimension of the computational cells in the streamwise direction
$\Delta y, \Delta z$ = dimensions of the computational cells along the cross-flow coordinates
Γ_1 = boundary surface with Dirichlet boundary conditions
Γ_2 = boundary surface with Neumann boundary conditions
φ = pseudo-pressure
ν = kinematic viscosity
ρ = density
τ = wall-tangent unit-vector
τ_w = average wall shear-stress
ψ = generic scalar quantity
Ω = domain (open set)
$\bar{\Omega}$ = domain including boundary, $\bar{\Omega} \equiv \Omega \oplus \Gamma_1 \oplus \Gamma_2$

Subscripts

f = face of control volume
w = quantity at the wall
0 = initial conditions

Superscripts

$'$ = fluctuating quantity
n = time level
$\overline{}$ = time- and streamwise-averaged quantity
$\langle\ \rangle$ = time- and volume-averaged

Introduction

The influence of secondary motions on convective heat transfer is relevant in several technical applications, for instance, in turbulent flows over corrugated surfaces (Nobile *et al.*, 2000b). We are interested in the thermal effects of the so-called secondary motions of the second kind, as first defined by Prandtl (1926), who recognized the existence of fluid motions on a cross-stream plane, induced by the presence of corners in solid boundaries. Buoyancy forces are neglected in the present study, so that the temperature field behaves like a passive scalar.

Secondary motions of the second kind are present only in a turbulent flow field (Gessner and Jones, 1965; Huser and Biringen, 1993) and it is well known that they are induced by anisotropic turbulent fluctuations in regions of isotach curvature (Gessner, 1972). These motions are relatively weak, in that they account only for $2 \div 3$ per cent of the bulk velocity; however, their influence on shear stress distribution and heat transfer rates is known to be quite significant (Huser and Biringen, 1993).

In this work, we adopt direct numerical simulation (DNS) as a convenient tool for studying both the velocity and the temperature fields in the presence of solid corners. A square duct is a suitable geometry in this respect. An imposed mean pressure gradient drives the flow, while a temperature difference is maintained between the horizontal walls. The vertical walls are assumed perfectly insulated. The Reynolds number, based on hydraulic diameter and bulk velocity, is approximately 4400, while the Prandtl number is assumed 0.71, representative of air.

Previous DNS studies for the turbulent flow in a square duct (Gavrilakis, 1992; Huser and Biringen, 1993) were focused upon the fluid dynamic features, and did not consider heat transfer.

Several validation tests were performed in order to ascertain the ability of the present finite volume methodology to simulate complex time-dependent flows. In detail, a fully-implicit version of the algorithm was tested by simulating a two-dimensional lid-driven cavity flow, at $Re = 1000$, based on the lid-velocity and the cavity height. The results show very good agreement with available benchmark calculations. The time-accuracy of the present method is determined by the combined influence of the time-discretization of the momentum equations, the fractional-step method adopted in this work, and the approximate-factorization scheme, used for an efficient solution of both the momentum and the energy equations. Even though all these approximations are assumed to be second-order time-accurate, first-order errors are introduced at the solid boundaries. They are known to affect the pressure field (Gresho, 1990), but they were also believed to be unimportant far away from the boundary. In this paper we show that, under certain circumstances, this may not be the case. Moreover, the first-order error introduced by the approximate-factorization technique affects the velocity field, even in the interior of the computational domain. This finding was unexpected.

The *OpenMP* parallel programming language was used to speed-up the calculations on shared-memory computers. We tested the parallel version of the code on up to eight CPUs, obtaining satisfactory performances.

From the present simulations, the maximum mean velocity, in the cross-flow plane, was found to be about 1.6 per cent of the centerline velocity. However, the results clearly indicate that, even if both the heat transfer rate and the friction factor are not strongly affected by the secondary motions, the effect on the distribution of various quantities within the flow field cannot be neglected. For instance, we report the distributions of both the shear stress and the heat flux, at the warm wall. Interesting features, clearly connected with the mean secondary motions, characterize these quantities.

Problem definition and scales

The full, time-dependent, incompressible Navier–Stokes and energy equations are solved directly, without any modelling assumption regarding the turbulent velocity and temperature fields. Simplifying assumptions are made, in that viscous energy dissipation and buoyancy forces are neglected, and the fluid properties are assumed constant. The hydraulic diameter D_h, the friction velocity u_τ and the wall-temperature difference ΔT_w are used to define dimensionless quantities. The domain dimensions are indicated in Figure 1, which shows a sketch of the duct. The non-dimensional conservation equations

of mass, momentum and energy describe the evolution of velocity, pressure and temperature fields:

$$\frac{\partial \mathbf{u}}{\partial t} + \nabla\cdot(\mathbf{uu}) = \frac{1}{Re_\tau}\nabla^2\mathbf{u} - \nabla p + 4\mathbf{i} \tag{1}$$

$$\nabla\cdot\mathbf{u} = 0 \tag{2}$$

$$\frac{\partial T}{\partial t} + \nabla\cdot(\mathbf{u}T) = \frac{1}{Re_\tau \mathrm{Pr}}\nabla^2 T \tag{3}$$

The velocity field is subject to no-slip boundary conditions at the solid walls, while the temperature is assumed constant and uniform on the horizontal walls, with a temperature difference maintained between them. The vertical walls are assumed thermally insulated, and all variables are assumed periodic in the streamwise direction, with a period equal to the streamwise domain length. The last term in the momentum equation represents the non-dimensional imposed pressure gradient.

Numerical methods

Equations (1)–(3) were solved by a finite volume algorithm. In order to describe the characteristics of the method, we first address the problem of separating the integration of the momentum equations from the continuity equation. Next, the spatial and temporal discretizations are discussed.

Fractional-step method

For incompressible flows, it is convenient to split the solution of the momentum equations from the continuity equation. Reasons for this are clearly explained by Comini (2001), and can be summarized by observing that it does not exist as an evolutionary equation for the pressure field. A Poisson equation for pressure can be obtained (Pope, 2000), and could be solved simultaneously with the

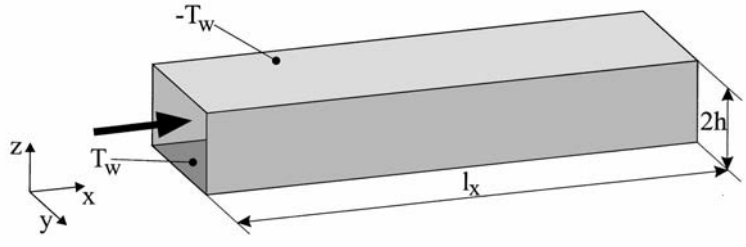

Figure 1.
Sketch of the computational domain

momentum equations. If the coupled system of momentum and pressure equations were exactly satisfied, the velocity field would result divergence-free.

However, as pointed out by Comini, the mass-conservation constraint would not be imposed directly, which could lead to the violation of continuity in a discrete framework. Moreover, boundary conditions for the pressure equation have to be obtained from the momentum equations and are not straightforward to be satisfied. So, alternative approaches are followed, in practice. In this respect, in our computations we employed the Projection 2 fractional-step method proposed by Gresho (1990). In principle, it leads to second-order accuracy in time for the velocity field, while first-order accuracy is achieved in the computation of the pressure field (Gresho, 1990; Brown *et al.*, 2001). We tested alternative formulations of the Projection method proposed by Gresho (1990), including improved boundary conditions for the intermediate velocity field, and an improved pressure update, as suggested by Kim and Moin (1985) and in Brown *et al.* (2001). Results of extensive numerical tests on these alternative approaches lead us to adopt the Projection 2 method as proposed by Gresho (1990).

Higher-order fractional-step methods have not been considered in the present work, for several reasons. First, the approximate-factorization (AF) technique used to solve the momentum equations is inherently second-order accurate in time in the interior of the computational domain, declining to first-order at the solid boundaries. Moreover, the maximum allowable time-step is subject to stability limits, due to the explicit representation of the advective term in the momentum equations. It turns out that this limit is quite stringent, so that its satisfaction leads automatically to accurate results. In addition, we are interested in the simulation of fully-developed flows, so that transitional phenomena, which usually require more accurate time-discretizations, are of no interest here.

The continuous version of the Projection 2 method is presented next; the selected boundary conditions were used for the simulation of the turbulent square duct flow.

1. Given $\mathbf{u}_0$, $\nabla\cdot\mathbf{u}_0 = 0$ in $\bar{\Omega}$, and $p^* = p(-t_f/2)$
2. Obtain an intermediate velocity field, $\mathbf{u}^*$, by solving a modified version of the momentum equations for $0 < t \leq t_f$:

$$\frac{\partial \mathbf{u}^*}{\partial t} = -\nabla p^* + \frac{1}{Re_\tau}\nabla^2\mathbf{u}^* - \nabla\cdot(\mathbf{u}^*\mathbf{u}^*) + \mathbf{f}^* \tag{4}$$

$$\mathbf{u}^* = \mathbf{w} \text{ on } \Gamma_1 \tag{5}$$

$$\mathbf{u}^*(x + l_x\mathbf{i}) = \mathbf{u}^*(x) \ \forall x \tag{6}$$

3. Evaluate the pseudo-pressure, which projects $\mathbf{u}^*$ onto the divergence-free vector field (Gresho, 1990):

$$\nabla^2\varphi = \nabla\cdot\mathbf{u}^* \text{ in } \Omega, \text{ at time } t_f \tag{7}$$

$$\frac{\partial\varphi}{\partial n} = 0 \text{ on } \Gamma_1$$

$$\varphi(x + l_x\mathbf{i}) = \varphi(x) \ \forall x$$

4. Project the velocity field:

$$\mathbf{v} = \mathbf{u}^* - \nabla\varphi \text{ in } \bar{\Omega} \tag{8}$$

5. Impose the actual boundary conditions to the velocity field $\mathbf{v}$ on Γ_1:

$$\mathbf{v} = \mathbf{w}_{t=t_f} \text{ on } \Gamma_1 \tag{9}$$

6. Update the pressure field:

$$p_{t=t_f/2} = p^* + \varphi/t_f \tag{10}$$

and start a new cycle, by letting $\mathbf{u}_0 \leftarrow \mathbf{v}$, $p^* \leftarrow p_{t=t_f/2}$ in $\bar{\Omega}$.

Some remarks are worthwhile, at this point. First, $\mathbf{u}^*$ is a second-order approximation of $\mathbf{u}_{t=t_f}$ in $\bar{\Omega}$, as shown by Gresho (1990). The pseudo-pressure is related to the pressure field by:

$$\varphi = t_f^2\frac{\partial p}{\partial t}\bigg|_{t=0} + F + O(t_f^3) \text{ in } \bar{\Omega} \tag{11}$$

Gresho (1990) proved that F is a harmonic function of order t_f^2, satisfying the following boundary-value problem:

$$\nabla^2 F = 0 \text{ in } \Omega$$

$$\frac{\partial F}{\partial n} = -t_f^2\frac{\partial}{\partial n}\frac{\partial p}{\partial t}\bigg|_{t=0} + O(t_f^3) \tag{12}$$

Moreover, what is most important, $\mathbf{v}$ is a second-order approximation of $\mathbf{u}_{t=t_f}$ (Gresho, 1990). In Brown *et al.* (2001), it is shown that better boundary conditions could be applied to $\mathbf{u}^*$. Namely, the boundary condition (5) causes a slip velocity to occur on Γ_1, which is artificially eliminated after the projection step, creating a discontinuity in the velocity field $\mathbf{v}$. As explained by Gresho (1990), the elimination of the slip velocity after the projection step (8) corresponds to a discontinuous flux of tangential vorticity from the boundary

Γ_1 into the computational domain. Kim and Moin (1985) and Brown *et al.* (2001) suggest eliminating the slip velocity by applying the following tangential boundary conditions for $\mathbf{u}^*$ on Γ_1:

$$\mathbf{u}^* \cdot \boldsymbol{\tau} = \mathbf{w} \cdot \boldsymbol{\tau} + \frac{\partial \varphi^n}{\partial \boldsymbol{\tau}} \quad \text{on} \quad \Gamma_1 \tag{13}$$

By using Equation (13) one obtains second-order accuracy for the velocity field in the Projection 1 framework (Brown *et al.*, 2001), while it does not affect the order of accuracy of the Projection 2 method. This is reasonable, in that the slip velocity resulting from the application of the standard Projection 2 algorithm is a second-order quantity in t_f:

$$s = (\mathbf{v} - \mathbf{w}) \cdot \boldsymbol{\tau} = -t_f^2 \frac{\partial p}{\partial t}\bigg|_{t=0} + O(t_f^2) \quad \text{on} \quad \Gamma_1 \tag{14}$$

However, Armfield and Street (2001) show that the use of Equation (13) with the Projection 2 method causes a relevant reduction in the magnitude of the error on the evolution of pressure, even though it does not affect the order of accuracy.

The pressure-update, Equation (10), is obtained by:

$$\begin{aligned} \frac{p(t_f/2) - p(-t_f/2)}{t_f} &= \frac{\partial p}{\partial t}\bigg|_{t=0} + O(t_f^2) \\ &= \frac{\varphi}{t_f^2} + O(1) \end{aligned} \tag{15}$$

so that

$$p(t_f/2) = p(-t_f/2) + \frac{\varphi}{t_f} + O(t_f) \tag{16}$$

The $O(t_f)$ error arises from the function F; far away from the boundary, F should be $O(t_f^3)$ (Gresho, 1990), so that the error on $p(t_f/2)$ should be $O(t_f^2)$ in the interior of the domain. Kim and Moin (1985) and Brown *et al.* (2001) suggest a second-order update for the pressure field, in the framework of semi-implicit methods, when the viscous term in Equation (4) is discretized by the Crank–Nicolson method. When applied to the Projection 2 method, this update reads:

$$p^{n+1/2} = p^{n-1/2} + \frac{\varphi}{t_f} - \frac{1}{2Re_\tau} \nabla^2 \varphi \tag{17}$$

The improved pressure-update does not significantly affect the accuracy of the velocity field, which is still second-order accurate in time (Brown *et al.*, 2001).

Spatial discretization

The present algorithm adopts a traditional MAC staggered-grid arrangement for the flow-field variables (Ferziger and Perić, 1999). Nodes for scalar variables, like pressure and temperature, are located at the control volume (CV) center, while the mid-point of each CV-face is selected for the location of the velocity component normal to the face itself. Figure 2 shows such a variables arrangement in the two-dimensional case.

Among other advantages (Patankar, 1980; Ferziger and Perić, 1999), the use of both a staggered-grid and a direct Poisson solver guarantees mass-conservation, for each CV, up to round-off error. In the framework of the adopted projection method, this is achieved as follows:

Continuous case

(1) Conservation requirement:

$$\int_{\Delta S} \mathbf{u} \cdot n \; \mathrm{d}S = 0 \tag{18}$$

(2) Conservation error *before* the projection step:

$$\epsilon = \int_{\Delta S} \mathbf{u}^* \cdot n \, \mathrm{d}S \neq 0 \tag{19}$$

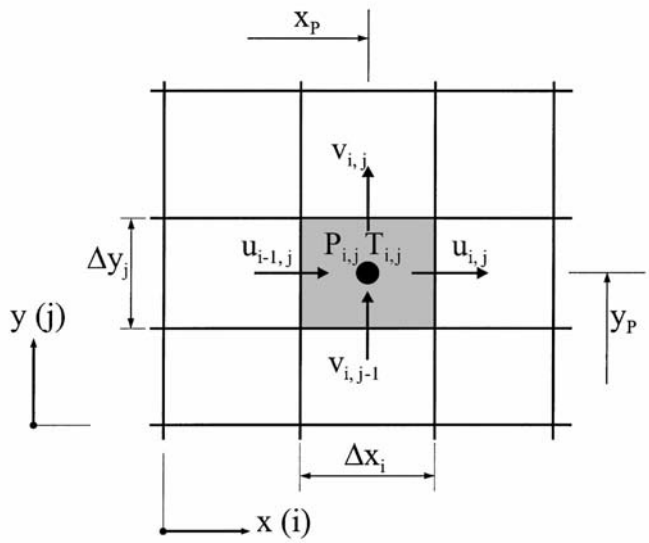

Figure 2.
Staggered grid for the two-dimensional case

(3) Projection step:

$$\int_{\Delta S} (\mathbf{u}^* - \nabla\phi)\cdot n \ \mathrm{d}S = 0 \Longleftrightarrow \int_{\Delta S} \nabla\phi\cdot n \ \mathrm{d}S = \int_{\Delta S} \mathbf{u}^*\cdot n \ \mathrm{d}S \tag{20}$$

Discrete case

(1) Conservation requirement:

$$\sum_f u_f \, \Delta S_f = 0 \tag{21}$$

(2) Conservation error before the projection step:

$$\epsilon = \sum_f u_f^* \, \Delta S_f \neq 0 \tag{22}$$

(3) Projection step:

$$\sum_f (u_f^* - \delta_f \phi) \ \Delta S_\mathrm{f} = 0 \Longleftrightarrow \sum_f \delta_f \phi \, \Delta S_\mathrm{f} = \sum_f u_f^* \ \Delta S_\mathrm{f} \tag{23}$$

where ΔS represents the CV surface, ΔS_f its generic face, and δ_f represents the discrete approximation of the normal derivative to face f.

The FV method solves directly Equation (23), and due to the staggered grid arrangement, no interpolation is required for the velocity components u_f. In our code we adopt second-order, central differentiation and interpolation schemes. Surface integrals, required for the evaluation of both the advective and diffusive fluxes, were calculated by the mid-point rule. The overall accuracy was verified to be second-order. One additional advantage of the FV method, when coupled with a staggered-grid approach, is that kinetic energy is automatically conserved.

Temporal discretization

Most of our computations have been performed by the Projection 2 method as presented by Gresho (1990), by exploiting an explicit second-order Adams–Bashforth extrapolation for the advective term and an implicit Crank–Nicolson scheme for the viscous term. The implicit treatment of the viscous term eliminates the stability constraint related to viscous diffusion.

The semi-discrete version of the fractional-step algorithm adopted in this work consists of the following steps:

(1) Given $\mathbf{u}_0$, $\nabla\cdot\mathbf{u}_0 = 0$ in $\bar{\Omega}$ and $\mathbf{u}_0\cdot n = \mathbf{w}\cdot n$ on Γ_1

(2) Perform one time-step by a Projection 1 method. This allows to set the initial pressure field: $p(\Delta t/2) \approx \varphi/\Delta t$

(3) Solve for the intermediate velocity field $\mathbf{u}^*$:

$$\frac{\mathbf{u}^* - \mathbf{u}^n}{\Delta t} = -\nabla p^{n-1/2} + \frac{1}{2Re_\tau}[\nabla^2\mathbf{u}^* + \nabla^2\mathbf{u}^n] - \tfrac{1}{2}[3\mathbf{H}^n - \mathbf{H}^{n-1}] + \mathbf{f}^{n+1/2} \tag{24}$$

$$\mathbf{H}^n = \nabla\cdot(\mathbf{u}^n\mathbf{u}^n)$$

$$\mathbf{u}^* = w \text{ on } \Gamma_1, \quad \mathbf{u}^* \text{ periodic in } x$$

(4) Evaluate the pseudo-pressure, by solving:

$$\nabla^2\varphi = \nabla\cdot\mathbf{u}^* \tag{25}$$

$$\frac{\partial\varphi}{\partial n} = 0 \text{ on } \Gamma_1, \quad \varphi \text{ periodic in } x$$

(5) Update $\mathbf{u}^n$, by projecting $\mathbf{u}^*$ onto the divergence-free subspace:

$$\mathbf{u}^{n+1} = \mathbf{u}^* - \nabla\varphi \text{ on } \bar{\Omega} \tag{26}$$

The updated velocity $\mathbf{u}^{n+1}$ is a second-order approximation of the true velocity, since all the approximations are second-order accurate. In order to eliminate the slip-velocity at the wall, $\mathbf{u}^{n+1}\cdot\boldsymbol{\tau}$ is set to 0 on the no-slip walls: $\mathbf{u}^{n+1}\cdot\boldsymbol{\tau} = \mathbf{w}\cdot\boldsymbol{\tau}$ on Γ_1

(6) Update the pressure-field, by using a first-order accurate estimate:

$$p^{n+1/2} = p^{n-1/2} + \varphi/\Delta t \tag{27}$$

(7) After updating the velocity and pressure fields, the simulation is restarted from point 3.

The temperature field is solved independently of the velocity field, due to the explicit treatment of velocity in the energy equation.

The solution of step 3 is carried out by an AF technique, which decouples the solution of the momentum equations along each independent coordinate direction, while retaining the second-order accuracy in time. The same strategy is used for the energy equation. The implicit term of the momentum equations can be factorized as follows:

$$\left\{1-\frac{\Delta t}{2Re_\tau}\nabla^2\right\}u_i^* = \left\{1-\frac{\Delta t}{2Re_\tau}\frac{\partial^2}{\partial x^2}\right\}\left\{1-\frac{\Delta t}{2Re_\tau}\frac{\partial^2}{\partial y^2}\right\} \times\left\{1-\frac{\Delta t}{2Re_\tau}\frac{\partial^2}{\partial z^2}\right\}u_i^* + O[(\Delta t)^2] \tag{28}$$

Thus, the solution of step 3 progresses as follows:

$$\left\{1-\frac{\Delta t}{2Re_\tau}\frac{\partial^2}{\partial x^2}\right\}\hat{u}_i = -\nabla p^{n-1/2}\Delta t - \frac{\Delta t}{2}[3H_i^n - H_i^{n-1}] + \frac{\Delta t}{2Re_\tau}\nabla^2 u_i^n + f_i^{n+1/2} + u_i^n \tag{29}$$

$\hat{u}_i$ periodic in x

$$\left\{1-\frac{\Delta t}{2Re_\tau}\frac{\partial^2}{\partial y^2}\right\}\tilde{u}_i = \hat{u}_i \tag{30}$$

$\tilde{u}_i = 0$ on the vertical walls

$$\left\{1-\frac{\Delta t}{2Re_\tau}\frac{\partial^2}{\partial z^2}\right\}u_i^* = \tilde{u}_i \tag{31}$$

$u_i^* = 0$ on the horizontal walls.

The energy equation is solved by three similar steps:

$$\left\{1-\frac{\Delta t}{2Re_\tau \mathrm{Pr}}\frac{\partial^2}{\partial x^2}\right\}\hat{T} = -\frac{\Delta t}{2}[3H_i^n - H_i^{n-1}] + \frac{\Delta t}{2Re_\tau Pr}\nabla^2 T^n + T^n \tag{32}$$

$\hat{T}$ periodic in x

$$\left\{1-\frac{\Delta t}{2Re_\tau Pr}\frac{\partial^2}{\partial y^2}\right\}\tilde{T} = \hat{T} \tag{33}$$

$\partial\tilde{T}/\partial n = 0$ on the vertical walls

$$\left\{1-\frac{\Delta t}{2Re_\tau Pr}\frac{\partial^2}{\partial z^2}\right\}T^{n+1} = \tilde{T} \tag{34}$$

$T^{n+1} = \pm T_\mathrm{w}$ on the horizontal walls.

The boundary conditions for $\hat{u}_i$ and $\hat{u}_i$ are assumed to coincide with those imposed on u_i^*. This practice can be justified by observing that both $\hat{u}_i$ and $\hat{u}_i$ are first-order approximations of u_i^*. Thus, a first-order error is introduced at the solid boundaries. Similar considerations hold for the energy equation.

The Poisson equation arising from step 4 is solved by an efficient matrix-decomposition technique, based on ideas proposed by Babu and Korpela (1993). The fast fourier transform (FFT) is used to decouple the system of algebraic equations, resulting from a finite volume representation of Equation (25), along the streamwise, periodic direction.

A fully-implicit version of the present algorithm, using a Crank–Nicolson discretization for both the advective and the diffusive terms, was tested by simulating a lid-driven cavity flow at $Re = 1000$, where Re is the Reynolds number based on the lid-velocity and cavity height. The Projection 2 method was used, both in an iterative version, leading in principle to second-order accuracy for both the velocity and the pressure fields (Armfield and Street, 2001, 2002), and in the single-step version used for the square-duct simulation.

Two grids were used, 48×48 and 96×96, with hyperbolic-tangent stretching along both coordinate directions. Figure 3 shows the streamlines, evaluated on a 96×96 grid by the non-iterative method. The main parameters of the simulations are reported in Table I, together with the maximum discrepancy between the present results and those reported by Botella and Peyret (1998).

Figure 4 reports the L_∞ and L_1 time-discretization errors for the fully-implicit, iterative Projection 2 algorithm used to simulate the lid-driven cavity. Similar results were obtained by the semi-implicit algorithms. Figure 5 shows the same errors, obtained by the single-step Projection 2 (Gresho, 1990).

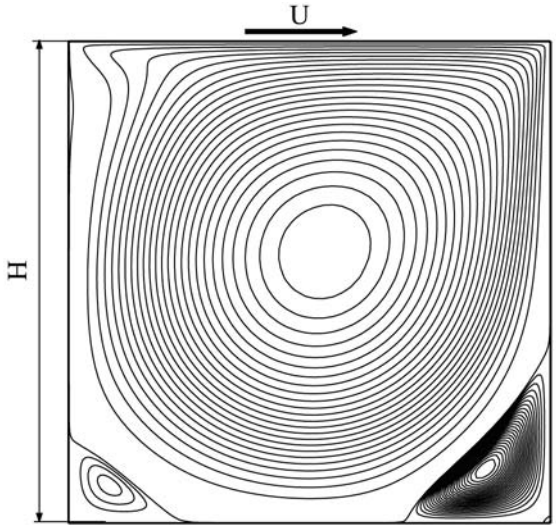

Figure 3.
Main geometric characteristics of the computational domain for the simulation of the lid-driven cavity. Streamlines at $Re = 1000$ evaluated on a 96×96 grid

The comparison of these figures leads to the following remarks:

- The iterative scheme leads to second-order convergence for both the velocity and the pressure fields, at points sufficiently far from the boundary. However, first-order convergence for both the velocity and the pressure fields is obtained at $x/H = y/H \approx 0.98$, that is, close to the moving top wall. As a consequence, the L_∞ errors, Figure 4(a), exhibit a first-order behaviour. The L_1 errors, Figure 4(b), indicate second-order accuracy for large Δt, but show first-order accuracy in the limit of very small time-steps. This behaviour is consistent with the fact that, as the time-step decreases, the first-order error contribution prevails.
- The iterative method is, in principle, second-order accurate. The only first-order contribution comes from the treatment of boundary conditions when using the AF technique. This has been verified to decrease the overall accuracy of the method.
- The Projection 2 method, Figure 5, obtains results very close to the iterative method. Again, the AF technique affects the accuracy of the velocity field, which otherwise would be expected second-order accurate. In this case, the pressure field is first-order accurate both in the interior of the domain and close to the boundary. The presence of round-off errors is evident in Figure 5(a), at the smallest values of the time-step, for the velocity at $(x/h = y/h = 0.15)$.
- It was verified that the pressure-update formula suggested by Kim and Moin (1985), Equation (17), in combination with the AF technique, did not affect significantly the accuracy of the velocity field, with respect to the simpler pressure-update formula, Equation (27). However, the accuracy of the pressure-field is reduced, and becomes first-order accurate even in the interior points.
- From the former remarks, it is evident that the first-order effect associated with the boundary conditions used in the AF framework, propagates onto the pressure field through the pseudo-pressure Equation (25), and the pressure-update Equation (27).

Armfield and Street (2001; 2002) performed the same tests on a differentially-heated cavity, where the flow was driven by buoyancy forces. They reported errors obtained with both the iterative and non-iterative Projection 2 algorithm, using various second- and third-order time-discretization schemes for the

Table I.
Maximum relative errors on horizontal and vertical velocity components for the lid-driven cavity at $Re = 1000$, evaluated on the vertical and horizontal bisectors, respectively

Grid	$\Delta x/H$, $\Delta y/H$	Δt	ϵ_u (%)	ϵ_v (%)
48×48	$0.0066 \div 0.0345$	0.0025	3.60	4.94
96×96	$0.0032 \div 0.0173$	0.0010	0.97	1.22

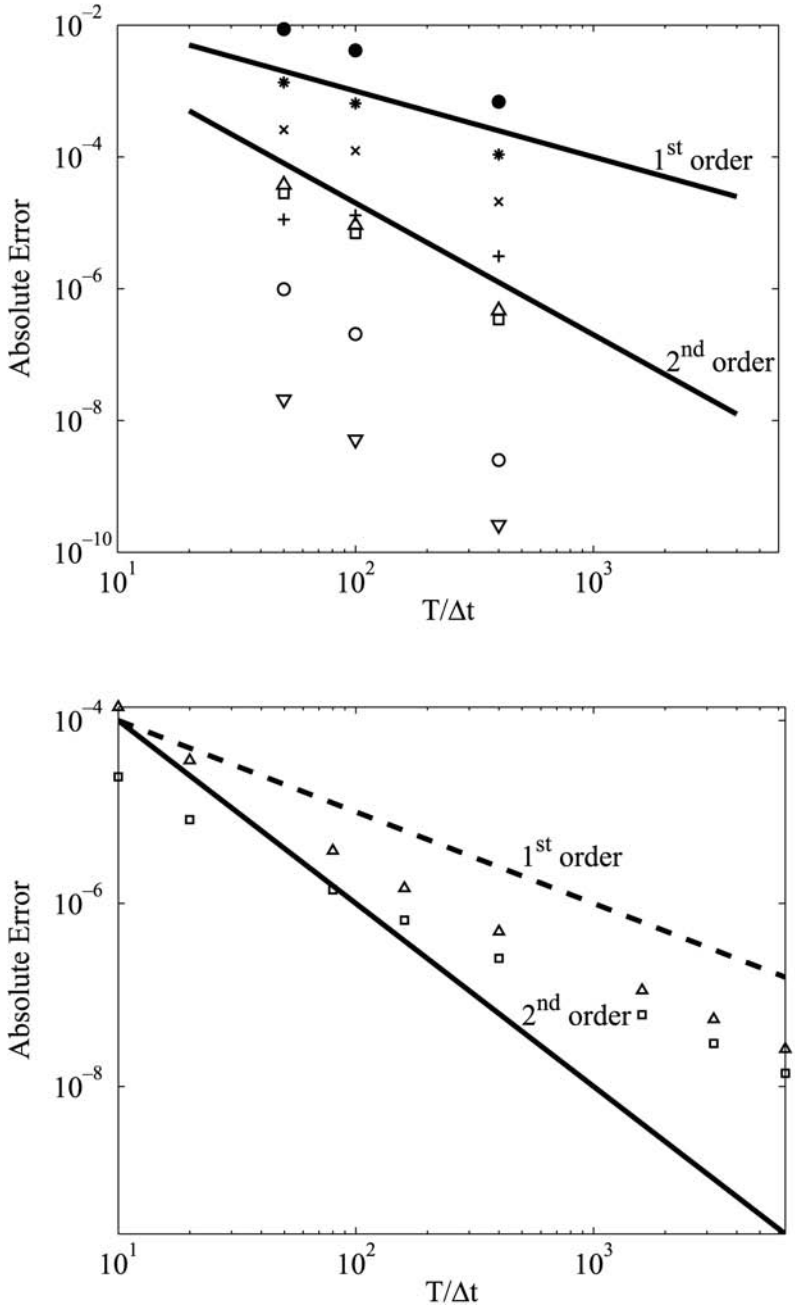

Figure 4. Time-discretization error for the lid-driven cavity flow at $Re = 1000$. Iterative Projection 2 method. (a) Absolute and L_∞ errors. □: L_∞ error on the horizontal velocity, with ADI. ∇: absolute error on the horizontal velocity at $x/H = y/H = 0.15$, with AF. +: absolute error on the horizontal velocity at $x/H = y/H = 0.98$, with AF. Δ: L_∞ error on pressure, with ADI. ○: absolute error on pressure at $x/H = y/H = 0.15$, with AF. ×: absolute error on pressure at $x/H = y/H = 0.98$, with AF. *: L_∞ error on the horizontal velocity, with AF. ●: L_∞ error on the pressure, with AF. (b) L_1 errors. △: L_1 error on horizontal velocity, with AF. □: L_1 error on pressure, with AF

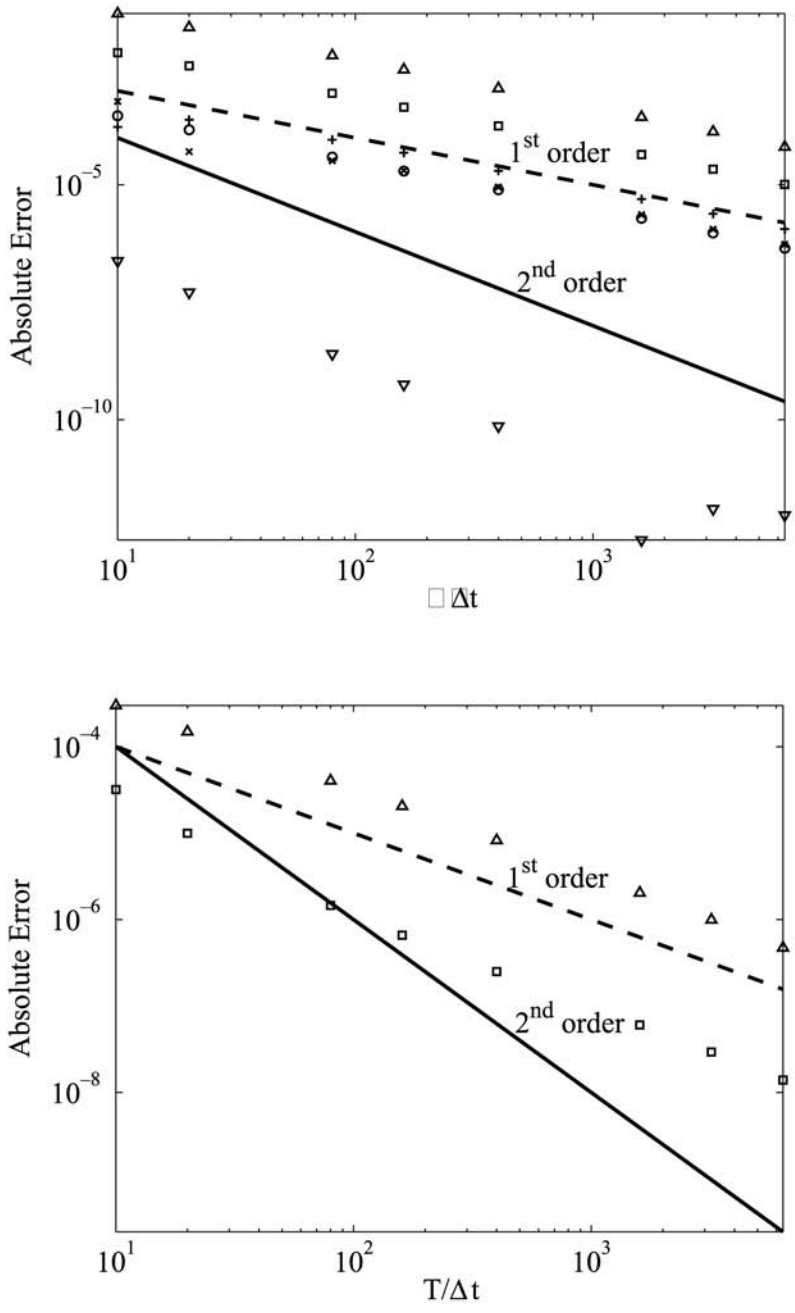

Figure 5.
Time-discretization error for the lid-driven cavity flow at $Re = 1000$. Projection 2 method. (a) Absolute and L_∞ errors. □: L_∞ error on the horizontal velocity. ▽: absolute error on the horizontal velocity at $x/H = y/H = 0.15$. +: absolute error on the horizontal velocity at $x/H = y/H = 0.98$. △: L_∞ error on pressure. ○: absolute error on pressure at $x/H = y/H = 0.15$. ×: absolute error on pressure at $x/H = y/H = 0.98$. (b) L_1 errors. △: L_1 error on horizontal velocity. □: L_1 error on pressure

advective and the diffusive terms. They observed the expected convergence rates for both the velocity and pressure fields, and report that the pressure-calculation was improved by the use of the Kim and Moin (1985) pressure-update formula. They used an alternate direction implicit (ADI) scheme in order to solve the modified momentum equations, when the advective term was discretized by explicit schemes. They explained the lower-order convergence-rates obtained by other investigators for the pressure field by observing that the pressure-update Equation (27) returns the pressure at time-step $n + 1/2$, so that, by comparing results obtained at a fixed final time by using different time-steps, an error of order Δt was introduced. They showed that, by extrapolating the pressure field to time-step $n + 1$, by using an Adams–Bashforth formula, the second-order convergence-rate was recovered. Our results were obtained by the suggested extrapolation, but different results were obtained, as already mentioned.

Since we suspected that the first-order convergence rate obtained for both the pressure and, particularly, the velocity field, was related to the inadequate representation of the boundary conditions by the AF technique, we also solved the modified momentum equation by an ADI method. By iterating the projection-step within each time-interval, as suggested by Armfield and Street (2001), we obtained second-order convergence for both velocity and pressure, on the whole domain. This can be verified in Figure 4. Therefore, the first-order convergence-rate for the velocity field, found in our results, is entirely due to the AF technique.

The three-dimensional simulations reported in this work were performed by exploiting a semi-implicit time-discretization scheme for the momentum equations. A second-order Adams–Bashforth scheme was used for the representation of the transverse advective terms, while the Crank–Nicolson scheme was used for the diffusive and the streamwise advective terms. Picard linearization (Ferziger and Perić, 1999) was adopted for the streamwise advective terms, thus relaxing the CFL limit.

The AF technique was used in order to split the integration of the momentum equations along the three coordinate directions. In spite of the main findings about the temporal accuracy, just discussed, the following considerations explain our choice:

(1) The ADI technique, differently than AF, requires an iterative solution. This is acceptable when the Poisson Equation (25) is solved by an iterative method, but can be too expensive if, as in our case, fast direct solvers are adopted. This is frequently the case for DNS studies.

(2) The ADI method requires several evaluations of right-hand-side of the momentum equations, and this further increases its computational cost.

(3) In the results section it will be shown that the time-step adopted in our simulations is orders of magnitude smaller than the Kolmogoroff

time-scale corresponding to the selected Reynolds number, so that the time-discretization error is negligibly small compared to the spatial-discretization error. Therefore, we can accept an *almost* first-order convergence rate in time, provided that the resulting algorithm is computationally efficient.

After time-discretization, the momentum and energy equations result in (ψ representing either u_i^* or T):

$$\frac{\psi^{n+1}-\psi^n}{\Delta t} = -\frac{\partial}{\partial x}(u^n\psi^{n+1}) - \frac{3}{2}\left[\frac{\partial}{\partial y}(v^n\psi^n) + \frac{\partial}{\partial z}(w^n\psi^n)\right] + \frac{1}{2}\left[\frac{\partial}{\partial y}(v^{n-1}\psi^{n-1}) + \frac{\partial}{\partial z}(w^{n-1}\psi^{n-1})\right] + \tfrac{1}{2}(\nabla^2\psi^{n+1} + \nabla^2\psi^n) + f^{n+1/2} \tag{35}$$

Parallelization

The *OpenMP* parallel programming language (OpenMP 2.0 2000) was used to run the code on shared-memory, parallel computer-servers and super-computers. Though the CFD community is presently oriented toward the development of distributed-memory *MPI* applications, which are usually more scalable, we believe that the *OpenMP* language can be very useful in some circumstances. More specifically, the *OpenMP* language is more widely applicable, since it can conveniently deal with algorithms that do not provide for a native partition of the data-structure. Both the AF and the matrix-decomposition algorithms used in our code are not optimal, in this respect. Moreover, *OpenMP* allows for simpler and progressive parallelization, and requires, in general, minor modifications to a scalar version of the code. In this sense, both the AF and the matrix-decomposition algorithms make the *OpenMP* parallelization very natural, in that blocks of planes can be solved independently, and are assigned to different processors. However, when the direction of integration is switched, for the AF method, and when the forward and backward transformations occur, for the matrix-decomposition method, a lot of communication takes place, so that an efficient distributed-memory implementation would be difficult. The *OpenMP* parallelization is not affected by these drawbacks, although performance and scalability are lower than the those provided by an efficient *MPI* implementation.

As an example, Table II illustrates values of the speed-up and CPU-time obtained, for a single time-step and with a grid $600 \times 127 \times 127$, on two different parallel computers, running the code in a multi-user, time-sharing environment. For the problem-size characterizing the simulations reported in this work, up to 10^7 cells, the performances summarized in Table II were deemed adequate.

Results and discussion

Two simulations have been considered, and they differ in the streamwise domain length, l_x. The computational grid is uniform in the homogeneous, streamwise direction, while an hyperbolic-tangent distribution is adopted in both cross-stream directions. The maximum expansion-ratio between adjacent cells is less than 6 per cent, so that the first-order error introduced by the grid stretching is negligible. The time-step was kept at a fixed value of $u_\tau \Delta t / D_\mathrm{h} = 0.00018$, which was judged to be adequate by Gavrilakis (1992). This leads to a CFL number around 0.2. The Kolmogoroff time microscale for the velocity field is of order $t_\mathrm{K} = 0.013 D_h / u_\tau$, so that $\Delta t / t_\mathrm{K} \approx 1.5 \times 10^{-2}$. Thus, we should be able to obtain an adequate time-resolution for most of the turbulent fluctuations. The analysis of the cumulative frequency distributions of both velocity and temperature signals, not shown here, confirmed this expectation, since most of the energy is contained in the resolved scales. In order to reduce the computational time required to loose information of the initial conditions, the streamwise advective term in both the momentum and energy equations was treated implicitly, and the time-step was doubled with respect to that used to acquire the statistics. The main parameters of both simulations are summarized in Table III.

Selecting an adequate streamwise domain-length is an important issue. As pointed out by Gavrilakis (1992), the correlation between two points, separated in the streamwise direction, shows a very slow decay, when compared with the plane-channel flow. This fact can be interpreted as the presence of very elongated turbulent structures, which we would like to capture. Moreover, (Gavrilakis, 1992) points out that a streamwise domain length of about $10\pi D_\mathrm{h}$ is sufficient to guarantee domain-independent statistics. Adopting such a domain would result in very expensive computations, so we use shorter computational boxes (Table III).

Table II. Performances obtained by running the semi-implicit code (only velocity and pressure fields) on two parallel computers: ORIGIN 3000, with 400 MHz processors, 8 Mb 2L cache; IBM SP3, with 222 MHz processors, 4 Mb 2L cache

	SGI Origin 3000		IBM SP3	
Nr CPUs	CPU-time (s)	Speed-up	CPU-time (s)	Speed-up
1	48.3	1	224.6	1
4	29.4	1.64	60.3	3.72
8	15.4	3.13	29.1	7.72

Table III. Main parameters for the simulations of the turbulent square duct

Case	l_x/D_h	$N_x \times N_y \times N_z$	Δx^+, Δy^+	$\Delta t\, u_\tau / D_\mathrm{h}$
A	18.84	$600 \times 127 \times 127$	9.42, $0.45 \div 4.59$	0.00018
B	6.28	$200 \times 127 \times 127$	9.42, $0.45 \div 4.59$	0.00018

Streamwise autocorrelation functions for streamwise velocity and temperature fluctuations, not reported here for brevity, were evaluated for both cases, A and B. At the centerline, for case A, the correlation functions for both streamwise velocity and temperature tend to oscillate around zero at separations much smaller than half of the domain length. This should indicate that the largest turbulent structures are contained within the computational domain. In the near-wall region, however, the autocorrelation functions do not vanish within half of the domain length. This behaviour is likely to be the effect of the very elongated streaky structures found in the near-wall region, which are well documented in the channel flow. Streamwise velocity and temperature streaks are illustrated in Figure 6. The autocorrelation functions for case B, however, indicated that the smaller length of the domain is inadequate to capture the largest turbulent structures, even in the core-region.

A clear similitude exists between streamwise velocity and temperature streaks, indicating that the Reynolds similarity holds, in the near-wall region.

Mean secondary motions in the cross-flow plane of the square duct, shown in Figure 7, result in four couples of counter-rotating corner-vortices, and they are well documented in the literature (Gavrilakis, 1992). Other four couples of weaker counter-rotating vortices are located on both sides of the wall-bisectors; they are relatively weak and highly intermittent, and are known to be a low-Reynolds effect (Huser and Biringen, 1993).

Mean temperature profiles, at several spanwise locations, are reported in Figure 8, together with a mean temperature profile for the plane channel flow. As can be recognized, the temperature profiles for the channel flow and for the duct flow, at the wall-bisector, agree almost perfectly over the whole channel height. This similarity could be explained by looking at the ensemble-averaged

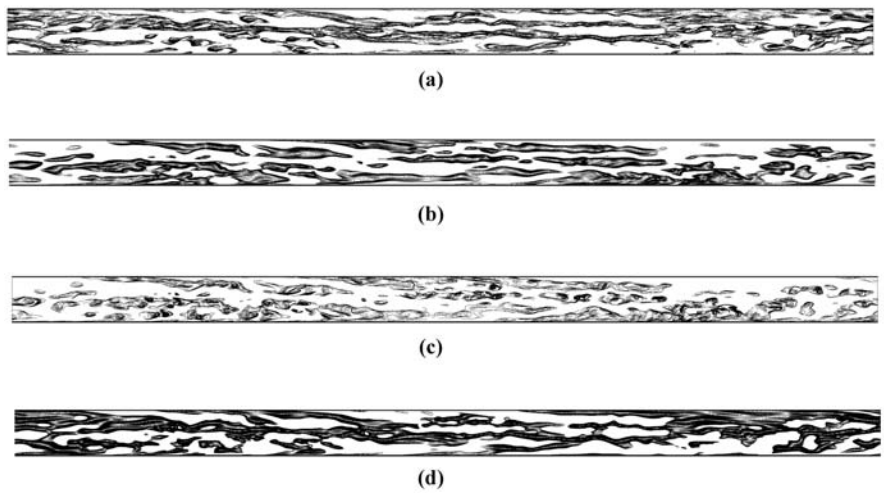

Figure 6.
Streamwise velocity and temperature fluctuations, at $z^+ \approx 17$, from case A. (a) negative velocity fluctuations; (b) positive velocity fluctuations; (c) negative temperature fluctuations; (d) positive temperature fluctuations

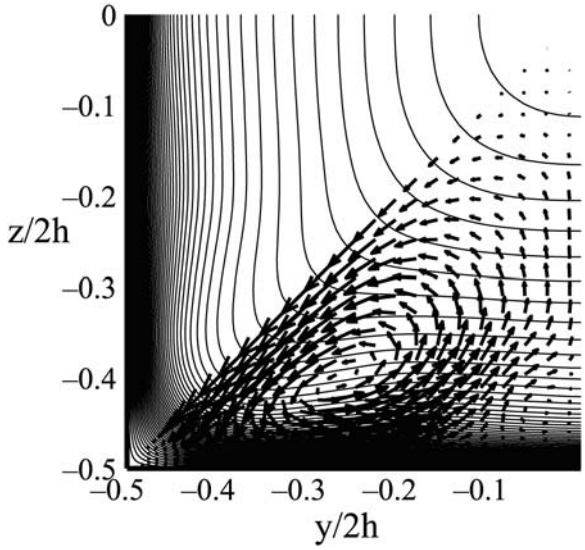

Figure 7.
Mean secondary motions on a cross-stream plane. Mean streamwise velocity contours are superimposed

energy equation for both the plane channel and the duct flows. Due to the imposed boundary conditions and to the symmetries, which must hold at the wall-bisector, the differences between the energy equation, in the two cases, are restricted to the following terms:

$$\bar{w}\frac{\partial}{\partial z}\bar{T} = \frac{1}{Re_\tau Pr}\left[\frac{\partial^2}{\partial z^2}\bar{T} + \frac{\partial^2}{\partial y^2}\bar{T}\right] - \frac{\partial}{\partial z}\overline{w'T'} \tag{36}$$

It was verified that the distributions of $\overline{w'T'}$ across the square duct and the channel are very similar, when evaluated at the wall-bisector. Since the turbulent heat flux decreases by approaching the side-walls, it is not surprising that a mean temperature distribution, evaluated at 3.3 wall-units from a side-wall (Figure 8), results in a less *bulged* profile, compared to the one at the wall-bisector. Maybe it is even more interesting to note that, at a distance of 36 wall units from a side-wall, this trend is inverted. From Figure 8, it is evident that the first term on the right-hand side of Equation (36) is negligible with respect to the third one. The curvature of mean temperature contours, on a wall-bisector, is also very small, so that the second term on the right-hand side can be neglected as well, as a first approximation. Moreover, from our data it results that the z-variation of the turbulent heat flux assumes larger values at 36 wall-units from a vertical wall, than at a wall-bisector. So, the fact that $\mathrm{d}T/\mathrm{d}z$ is smaller near a vertical wall, than at the centerline, can be explained only if $\bar{w}$ is larger at the first location, as was verified.

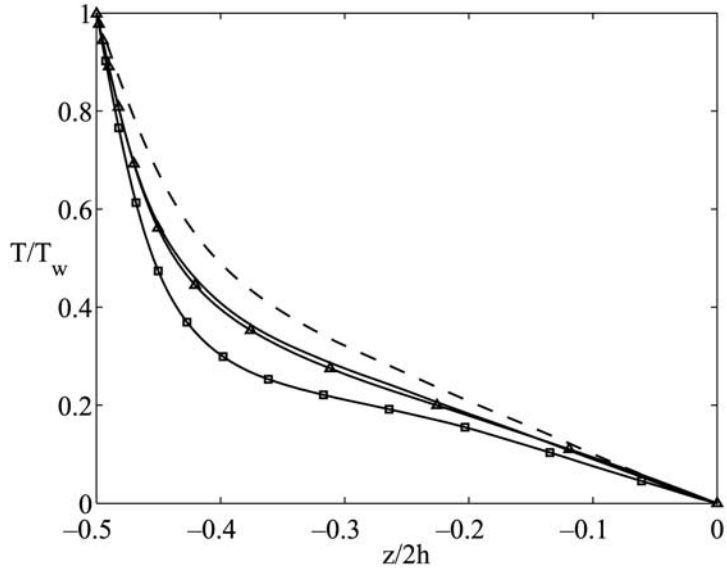

Figure 8.
Mean temperature profile at several spanwise locations, and data from a DNS for the plane-channel flow (Nobile *et al.*, 2000a). –: $y/2h = -0.4887$. –□–: $y/2h = -0.384$. ––: $y/2h = 0$ (centerline). –Δ–: plane-channel

Values for the bulk-Reynolds number, Re_b, the mean Nusselt number, Nu, the mean turbulent kinetic energy, $\langle k \rangle$, and the friction factor, C_f, are reported in Table IV. The friction factor agrees, to better than 1 per cent, with empirical correlations available for this geometry (Bhatti and Shah, 1987), when the laminar equivalent diameter, $D_l = (1 + \sqrt{2})\ h$, is used. The Nusselt number is defined as $\mathrm{Nu} = (q_w\, 2h)/[k(\Delta\, T_w)]$. The Nusselt number from present simulations is only 12 per cent smaller than the Nusselt number evaluated for the channel flow (Nobile *et al.*, 2000a).

A possible interpretation of this fact could be that the decrease of heat transfer in the laminar regions, close to the vertical walls, is partially compensated by the increase due to the presence of mean secondary motions. This picture is confirmed by Figure 9, which shows the total heat-flux profile, evaluated on spanwise sections. Focusing on locations near the vertical walls, one can appreciate that the total heat-flux is smaller in the core-region, than

Table IV.
Global statistics, compared with a DNS for the square duct, and the results for the channel flow

	Present results	Gavrilakis (1992)	Channel (Nobile *et al.*, 2000a)
Re_b	4443	4410	4602
U_b	14.8	14.7	15.3
$C_f \times 10^3$	9.135	9.25	8.2
$\langle k \rangle$	$2.0u_\tau^2$	$2.1u_\tau^2$	
Nu	5.55		5.45

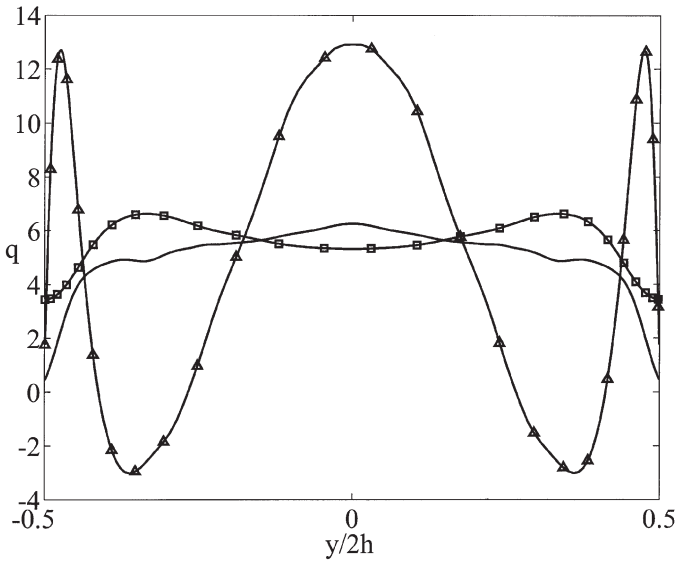

Figure 9.
Total heat flux profile at several distances from the bottom, warm wall. $-\square-$: $z/2h = -0.5$ (wall). $-\Delta-$: $z/2h = -0.377$. $--$: $z/2h = 0$ (centerline)

near the horizontal walls. This is due to the increased turbulent heat flux, caused by the corner vortices. No empirical formulae are available, to the best of our knowledge, for the Nusselt number, with the boundary conditions used in the present simulations.

Figure 10 shows the distribution of the mean, total shear stress at the bottom wall. The shear stress vanishes at the vertical walls, due to the presence of stagnation regions at the corners. Three local maxima are evident in the shear-stress profile at the wall. The near-wall peaks are located in the region below the corner-vortices, and are clearly generated by the intense impingement of high-speed fluid, carried from the vortex, against the wall. The local minima are located where the corner vortices carry low-speed fluid from the wall, toward the core region. Clustering and widening of streamwise velocity contours, evident in Figure 7, allow an immediate interpretation of the shear-stress behaviour.

The local heat flux at the horizontal wall, Figure 9, shows a behaviour similar to the shear stress. In this case, however, no central maximum is present.

A possible explanation of the heat-flux distribution at the wall can be formulated by means of a Lagrangian point of view. Let us consider a warm fluid particle, trapped into a vortex, and moving from the core region toward the upper, cold wall. Due to thermal diffusion, heat phleaks from the particle, during its motion through the progressively colder fluid regions, near the cold wall. Of course, the *leaking* of heat from a fluid particle takes place during a longer period, if the fluid particle is trapped into a weak vortex, like those

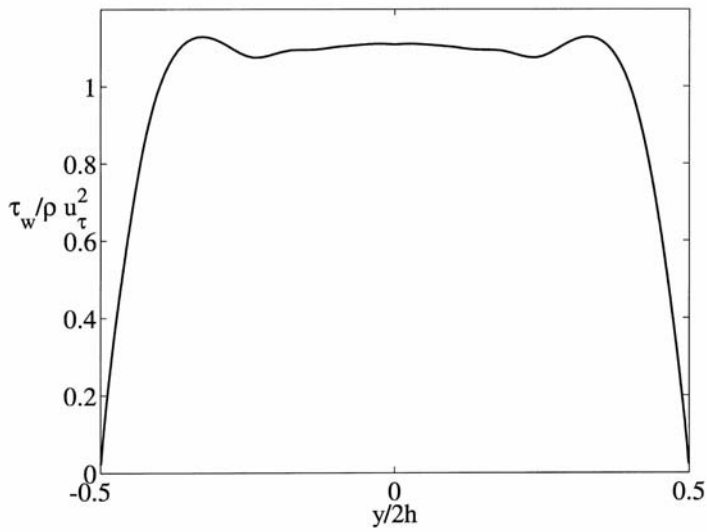

Figure 10.
Mean profile of shear-stress at an horizontal wall

located on both sides of wall bisectors. This picture can be applied to streamwise-momentum transfer as well. But, since $\mathrm{Pr} = 0.71 < 1.0$, we can expect momentum leaking out from a vortex less intensively than heat. This could account for the different distribution of heat flux and shear stress at the horizontal walls: the weak vortices, close to a wall bisector, do not have enough strength for avoiding sensible leak of heat from a fluid particle, but they are strong enough for carrying streamwise momentum toward the walls.

The $\overline{w'T'}$ turbulent heat flux decreases near the vertical walls, due to the combined effect of a reduction in the intensity of both w' and T', as shown in Figure 11. Moreover, there is also a loss of correlation between w' and T', in regions close to the vertical walls, as reported in Figure 12, which shows the distribution of $\overline{w'T'}/w'T'$. This is an expected feature, considering the different boundary conditions imposed on velocity and temperature.

It can be interesting to observe that the correlation coefficient is particularly low in correspondence of the corner vortices, close to the vertical walls, in regions where the fluid is *pumped* from the wall toward the core region. This feature could be related to the thickening of the region of low w', attached to the horizontal walls, when approaching the vertical walls (Figure 11). The reduction in w' would lead to an increased correlation coefficient. However, one can conjecture that the reduction in the turbulent heat flux, caused by the *loss of correlation* between w' and T' fluctuations, more than compensate for the reduction of w', resulting in a decreased correlation coefficient.

We have verified that the distributions of the turbulent and molecular heat fluxes, not reported here, are surprisingly similar. This may suggest that,

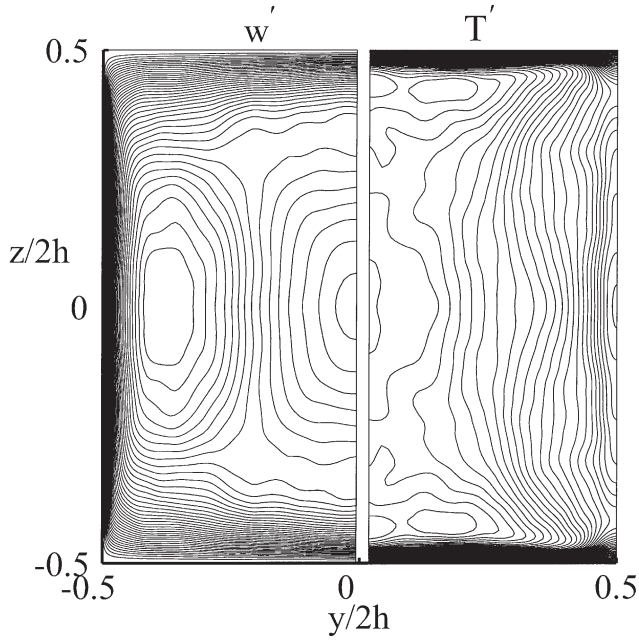

Figure 11.
w' and T' contours, on a cross-flow plane

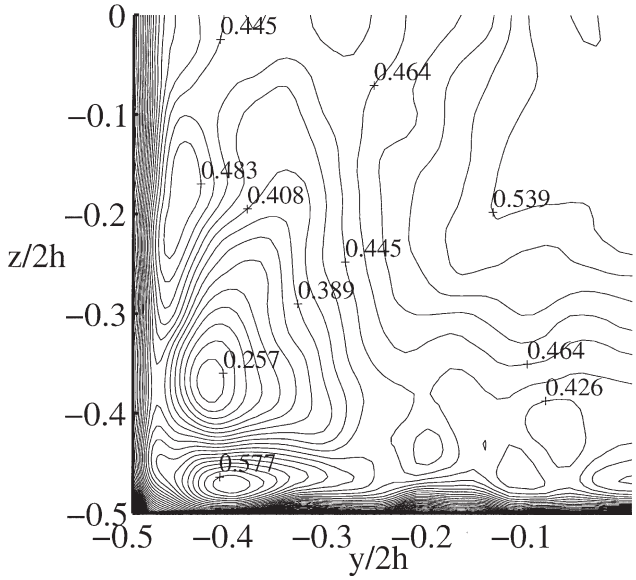

Figure 12.
$\overline{w'T'}/w'T'$ contours, on a cross-flow plane

unlike the isotropic eddy-viscosity approach for the velocity field, which is unable to reproduce i.e. the secondary motions, a gradient-diffusion model for the temperature field would provide an adequate representation of the turbulent heat flux. In order to test this idea, we defined an eddy-diffusivity as:

$$\alpha_{\mathrm{t}} = \frac{\overline{w'T'}}{\overline{\frac{\partial T}{\partial z}}} \tag{37}$$

where it should be noted that, with this definition, α_t is isotropic but not homogeneous. The *modelled* components of the turbulent heat-flux, are therefore given by:

$$q_y = \alpha_{\mathrm{t}} \frac{\partial T}{\partial y} \tag{38}$$

$$q_z = \alpha_{\mathrm{t}} \frac{\partial T}{\partial z} \tag{39}$$

There is no unique definition for α_{t}, in the duct-flow configuration. Namely, the molecular heat-flux is not exactly parallel to the turbulent heat-flux, on a duct cross-section. The definition (37) is motivated by the importance of exactly reproducing the main turbulent heat-flux $\overline{w'T'}$. That is, $q_z \equiv \overline{w'T'}$. However, Equation (38) is a *true model* for $\overline{v'T'}$, in the framework of eddy-diffusivity models. The modelled and computed heat-flux vector fields, $(q_y, q_z)^T$ and $(\overline{v'T'}, \overline{w'T'})^T$ respectively, (not reported here) have similar direction fields. Their magnitudes are compared in Figure 13, and the agreement is remarkably good. The maximum value for both distributions is 0.0281. So, quite surprisingly, eddy-diffusivity models, for this heat transfer problem, work pretty well.

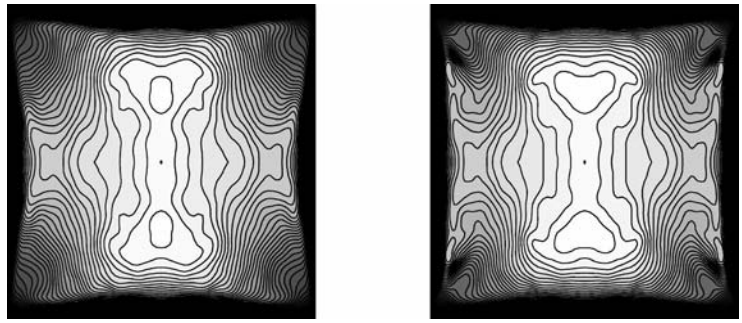

Figure 13.
(a) Magnitude of $(\overline{v'T'}, \overline{w'T'})^T$. (b) Magnitude of $(q_y, q_z)^T$. In both figures, brighter colours represent higher magnitudes

The distribution of α_t/α is shown in Figure 14. It is almost constant in the core-region, a circumstance that could suggest that assuming a uniform value of α_t in the core-region could result in a sufficiently good approximation, for practical purposes. In (Piller *et al.*, 2002) simple modelizations of α_t are shown to not affect significantly the evaluation of the mean-temperature profile, for the turbulent plane-channel flow. In the near-wall region turbulent heat-transfer is smaller than the combined effect of molecular and advective heat-transfer, so that a simple fitting of the α_t profile should be sufficient.

Streamwise, cumulative power spectra, for streamwise velocity and temperature fluctuations, are shown in Figure 15, at two locations along the bottom-wall bisector. One interesting feature arising from this figure is that, although the Prandtl number is smaller than unity, streamwise velocity fluctuations decay faster, at high wavenumbers, than temperature fluctuations, both in the core region and in the near-wall region. As for the core region, this feature could be explained by observing that the viscosity is relatively unimportant, here, so that large turbulent structures can be generated. So, in the core region, most of the energy should be concentrated in large-scale motions, corresponding to small wavenumbers. Possibly, due to $\mathrm{Pr} < 1$, the temperature field does not *follow* exactly these velocity structures, generating smaller-scale structures. As for the near-wall region, viscosity and molecular conductivity should dominate the momentum and heat transfer, respectively. Since $\mathrm{Pr} < 1$, the reported behaviour of spectra does not lead to a straightforward interpretation. In addition, both velocity and temperature

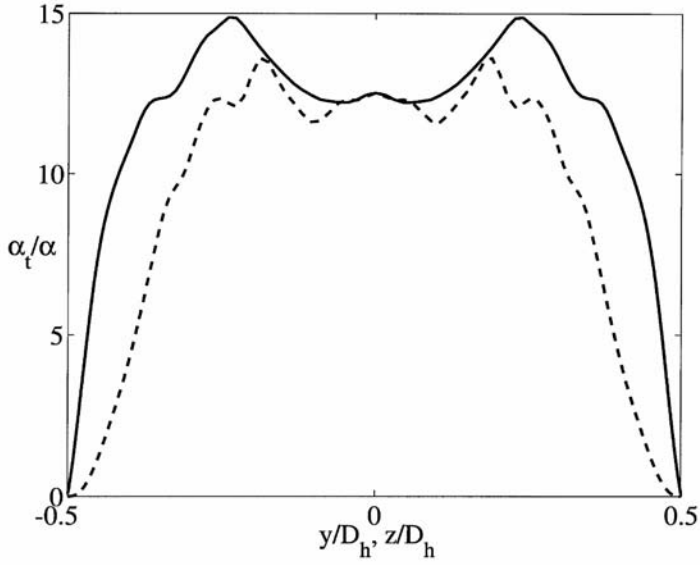

Figure 14.
Distribution of α_t/α along an horizontal bisector, solid line, and a vertical bisector, dashed line

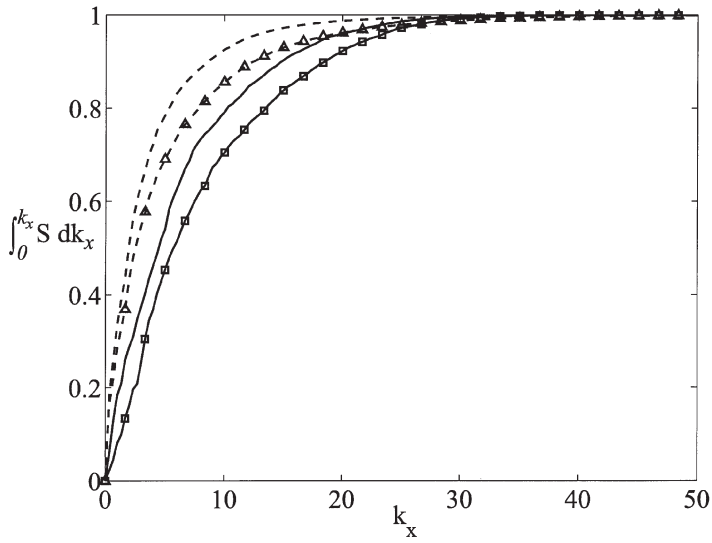

Figure 15.
Spectra of streamwise velocity and temperature fluctuations along the bottom-wall bisector. $--$: u' at $z/2h = 0$ (centerline). $--$: u' at $z/2h = -0.437$. $-\square-$: T' at $z/2h = 0$ (centerline). $-\Delta-$: T' at $z/2h = -0.437$.

fluctuations decay faster near the wall, than in the core region, as could be expected, due to the larger contribution of viscosity and thermal conductivity near the walls.

Concluding remarks

In this work we presented the results, obtained from DNS, of turbulent forced convection in a differentially-heated square duct. In particular, DNS results for the temperature field were not available before, to the best of our knowledge.

Streamwise cumulative spectra for both streamwise velocity and temperature fluctuations were calculated, at various cross-stream locations. Some peculiar aspects regarding the decay of the highest wave-number components were pointed out.

The influence of mean secondary motions on both the temperature and velocity fields was discussed. The maximum intensity of these motions was found to be about 1.6 per cent of the maximum mean streamwise velocity. The comparison of the duct flow with the plane-channel flow led to the observation that global parameters, like the Fanning friction-factor and the Nusselt number, are not strongly affected by the presence of the side-walls, while the distribution of the local shear-stress and heat-flux at a wall shows characteristic oscillations, whose origin appears to be related to the mean secondary motions.

The eddy-diffusivity approach, usually adopted in CFD predictions, is known to be unable to reproduce the most salient features for this bounded

flow, like for instance the secondary motions. However, quite surprisingly, this hypothesis seems to work well for the turbulent heat transfer.

The time-discretization procedure, used throughout this work, is quite common to other DNS and LES codes for simulating incompressible flows. The formal temporal accuracy is second-order for the velocity field, no matter what type of boundary conditions are used for the intermediate velocity field at the solid boundaries, and regardless the pressure-update formula (Armfield and Street, 2002). Following Gresho (1990), for the square channel simulations we adopted the simplest pressure-update formula (27), which leads to first-order accuracy of the pressure field (Armfield and Street, 2002). This is consistent with the use of the AF technique in these simulations, which makes useless the recourse to the second-order pressure-update formula. We experienced lower orders in the convergence of the results for the simulations of the two-dimensional lid-driven cavity. These effects were shown to originate at the solid boundaries, and to propagate deeply into the computational domain, at least in the two-dimensional lid-driven cavity flow, which is completely wall-bounded. The influence of the AF technique used to solve the modified momentum equations was explored by using an iterative version of the Projection 2 method (Armfield and Street, 2002). At each time-step, the converged velocity and pressure fields satisfy the true momentum equations to second-order accuracy, and the continuity equation exactly. However, by refining the time-step one observes second-order convergence only in the interior of the domain, while first-order convergence is attained near the boundaries. These effects have been shown to originate from the AF technique, since both the time-discretization and the iterative Projection 2 schemes are second-order accurate. Therefore, when higher-order time-accurate algorithms are needed, one is forced to abandon the AF technique.

The simulations of the weakly turbulent heat transfer in a square duct, reported here, involved up to 10 million cells. The size of the problem required using a parallel computer. The *OpenMP* algorithm proved to be adequate for medium-size problems, and showed satisfactory scalability up to eight processors.

References

Armfield, S. and Street, R. (2001), "The pressure accuracy of fractional-step methods for the Navier–Stokes equations on staggered grids", in *Proceedings 10th Biennial Computational Techniques and Applications Conference (CTAC2001)*, Brisbane, Australia.

Armfield, S. and Street, R. (2002), "An analysis and comparison of the time accuracy of fractional-step methods for the Navier–Stokes equations on staggered grids", *International Journal for Numerical Methods in Fluids*, Vol. 38, pp. 255-82.

Babu, V. and Korpela, S.A. (1993), "On the direct solution of Poisson's equation on a non-uniform grid", *Journal of Computational Physics*, Vol. 104, pp. 93-8.

Bhatti, M.S. and Shah, R.K. (1987), "Turbulent and transition flow convective heat transfer in ducts", in Kakaç, S., Shah, R.K., Aung, W., (Eds), *Handbook of Single-phase Convective Heat Transfer*, Chap. 4. Wiley, New York.

Botella, O. and Peyret, R. (1998), "Benchmark spectral results on the lid-driven cavity flow", *Computers and Fluids*, Vol. 27, pp. 421-33.

Brown, D.L., Cortez, R. and Minion, M.L. (2001), "Accurate projection methods for the incompressible Navier–Stokes equations", *Journal of Computational Physics*, Vol. 168, pp. 464-99.

Comini, G. (2001), "Equazioni della Convezione", in Comini, G., (Eds), *Fondamenti di Termofluidodinamica Computazionale*, (in Italian) SGE Editoriali, Padova pp. 1-37.

Ferziger, J.H. and Perić, M. (1999), *Computational Methods for Fluid Dynamics*, Second edition, Springer, Berlin.

Gavrilakis, S. (1992), "Numerical simulation of low-Reynolds number turbulent flows through a straight square-duct", *Journal of Fluid Mechanics*, Vol. 244, pp. 104-29.

Gessner, F.B. (1972), "The origin of secondary flow in turbulent flow along a corner", *Journal of Fluid Mechanics*, Vol. 58, pp. 1-25.

Gresho, P.M. (1990), "On the theory of semi-implicit projection methods for viscous incompressible flow and its implementation via a finite element method that also introduces a nearly consistent mass matrix. Part 1: theory", *International Journal of Numerical Methods in Fluids*, Vol. 11, pp. 587-620.

Gessner, F.B. and Jones, J.B. (1965), "On some aspects of fully developed turbulent flow in rectangular channels", *Journal of Fluid Mechanics*, Vol. 23, pp. 689-713.

Huser, A. and Biringen, S. (1993), "Direct numerical simulation of turbulent flow in a square duct", *Journal of Fluid Mechanics*, Vol. 257, pp. 65-95.

Kim, J. and Moin, P. (1985), "Application of a fractional-step method to incompressible Navier–Stokes equations", *Journal of Computational Physics*, Vol. 59, pp. 308-23.

Nobile, E., Piller, M. and Stalio, E. (2000a), "Direct numerical simulation of turbulent mixed convection in internal flows", *Proceedings U.I.T. 18th National Italian Conference on Heat-Transfer*, Vol. I, pp. 357-70 Milano (Italy).

Nobile, E., Stalio, E. and Piller, M. (2000b), "Numerical simulation of heat transfer over riblets", in, *Proceedings 3rd European Thermal Sciences Conference*, Hahne, E.W.P., Heidemann, W., Spindler, K., (Eds) Volume Vol. 1, pp. 313-8.

OpenMP FORTRAN 2.0 specification, http://www.openmp.org/specs/

Patankar, S.V. (1980), *Numerical Heat Transfer and Fluid Flow*, McGraw-Hill, New York.

Pope, S.B. (2000), *Turbulent Flows*, Cambridge University Press, Cambridge, U.K..

Prandtl, L. (1926), "Uber die ausgebieldete Turbulenz", in Verh. 2nd *Intl Kongr. f̈ur Tech. Mech.*, Zurich, English Transl. NACA Tech. Memo. 435, 63.

Piller, M., Nobile, E. and Hanratty, T.J. (2002), "DNS study of turbulent transport at low Prandtl numbers in a channel flow", *Journal of Fluid Mechanics*, Vol. 458, pp. 419-41.